Characterization of the High Temperature Strain Partitioning in Duplex Steels

Guilhem Martin, Daniel Caldemaison, Michel Bornert, Christophe Pinna, Yves Bréchet, Muriel Véron, Jean-Denis Mithieux, Thomas Pardoen

Characterization of the High Temperature Strain Partitioning in Duplex Steels

G. Martin · D. Caldemaison · M. Bornert · C. Pinna · Y. Bréchet · M. Véron · J.D. Mithieux · T. Pardoen

Abstract A microgrid technique has been developed for the analysis of the high-temperature micro-scale strain distribution between ferrite and austenite into duplex stainless steels. The local strain is measured by micro-extensometry using square microgrids engraved on flat specimens by electrolithography. The sample with microgrids on the surface and preliminary imaged with high definition scanning electron microscope (SEM), is inserted in a plane strain compression specimen to be deformed under conditions representative of hot rolling. After deformation, the sample is extracted from the compressed block and the surface is again analyzed by SEM and image processing to determine the strain field. The strain is heterogeneously distributed with a strong localization of the deformation, in the form of shear bands located within the ferrite and at the vicinity of the austenite/ferrite interphase boundaries. These strain maps provide useful informations about the rheology of the phases as well as about the local conditions at the origin of the damage process.

Keywords Microgrid technique · Duplex stainless steels · Strain partitioning · Micro-scale strain distribution · High temperature

G. Martin · Y. Bréchet · M. Véron
SIMaP (Laboratoire de Science et Ingénierie des Matériaux et Procédés), Groupe Physique du Métal, Grenoble-INP,
1130 rue de la piscine,
38402 Saint Martin D'Hères, France
e-mail: guilhem.martin@simap.grenoble-inp.fr

D. Caldemaison · M. Bornert
LMS (Laboratoire de Mécanique des Solides),
Ecole Polytechnique,
91128 Palaiseau, France

M. Bornert
Laboratoire Navier, Ecoles des Ponts ParisTech,
Université Paris-Est,
77455 Marne-la-vallée, France

C. Pinna
Department of Mechanical Engineering, IMMPETUS
(Institute for Microstructural and Mechanical Process Engineering:
The University of Sheffield),
Mappin Street,
Sheffield S1 3JD, UK

J. Mithieux
Service Métallurgie, APERAM Research Center BP 15,
62230 Isbergues, France

T. Pardoen
IMMC (Institute of Mechanics, Materials and Civil Engineering),
Université Catholique de Louvain,
Place Sainte Barbe 2,
1348 Louvain-la-Neuve, Belgium

Introduction

The Duplex Stainless Steels (DSS) constitute a family of stainless steels consisting of a two-phase microstructure involving δ-ferrite and γ-austenite. Exceptional combinations of strength and toughness together with good corrosion resistance under critical working conditions designate DSS as a suitable alternative to conventional austenitic and superaustenitic stainless steels. Such characteristics make these steels widely used in a variety of applications, particularly in oil and gas industries as well as in chemical containment applications [1]. However, the relatively poor hot workability of these alloys makes the industrial processing of flat products particularly critical. Cracking of the coils during hot rolling along the edges is frequently reported [2, 3]. As a consequence, additional operations like grinding, discontinuous processing, trimming or scraping are sometimes required, leading to a dramatic increase of the manufacturing costs.

The different metallurgical factors influencing the hot working behaviour of duplex stainless steels have been extensively investigated: volume fraction [4], size, and morphology [5] of both phases, softening mechanisms of the constituting phases [6–8], chemical composition [2, 9], mechanical properties of the interphase boundaries [10], and mechanical contrast between ferrite and austenite [3, 5, 11]. Strain measurements in DSS have already been studied at room temperature [12–14]. However, quantitative data about the high temperature strain partitioning between ferrite and austenite and strain heterogeneities induced by the microstructure are limited to preliminary experimental attempts [15–17] while being essential to unravel the origin of the damage mechanisms leading to the edge cracking process. Complex phenomena take place during hot forming of metals, especially when involving two phases with different strengths. Indeed, in addition to the overall stress and strain gradients, the local strain can be highly heterogeneous. A first method to quantitatively determine the strain partitioning has been proposed by Unckel [18] and used by Duprez et al. and Al-Jouni [3, 19]. These authors estimated the strain differences between the constituent phases by measuring the evolution of the dimensions of the grains. Other investigators have used hardness [20, 21] and residual stress measurements [13] to probe the relative strength of constitutive phases. In order to quantify the stress and strain partitioning in multiphase alloys, important research efforts have been recently made to obtain more accurate results. Grid techniques are often used in the context of metal forming, see examples in [22–24]. Microgrid techniques combined with SEM *in situ* mechanical testing and automated image analysis have been used for many years for the investigation of deformation mechanisms at the micro-scale [12, 25–31]. One advantage of the microgrid techniques is that they enable simultaneous observation of the microstructure and evaluation of the local strain field at the surface of a sample under loading. However, until recently, microgrid techniques could not be applied to deformation conditions representative of a hot rolling process. With the method initiated by Pinna et al. [15] and further developed by Hernandez [16] and Rupin [17], local deformation in steel samples can be measured at temperatures up to 1050°C. The latter technique has been adopted in this present work to investigate strain partitioning in duplex stainless steels. Note that strain partitioning can also be evaluated directly on the deformed microstructure if the contrast between the phases is large enough [32]. Interphase strain heterogeneities can also be mapped on materials on which a microgrid-type of marking is not possible when a sufficient intraphase image contrast is available, induced by a natural heterogeneity at a lower scale, an appropriate surface preparation or the use of specific imaging conditions [33]. However, because of the too low intraphase contrast in duplex steels and its potential strong evolution during hot deformation such grid-less techniques are not applicable for high temperature investigations.

The outline of the paper is the following. The materials and the experimental procedures are described in Section 2. Section 3 presents and discusses the experimental results, summarized in the conclusion.

Experimental Procedure

Material

The duplex stainless steel (DSS) has been supplied by Aperam in the hot rolled conditions. This grade does not correspond to any commercial DSS with chemical composition given in Table 1. It was selected because of its poor hot workability, associated to the generation of 50 mm long edge-cracks during the hot rolling process. The undeformed microstructure involves austenite flattened along the transverse direction embedded inside a ferrite matrix, see Fig. 1(a). The as-received material was annealed using an appropriate heat treatment in order to generate an equiaxed austenite morphology with an average grain size equal to about 60 μm [34], see Fig. 1(b). The average grain size of the ferrite was about 50 μm.

Procedures for High-Temperature Resistant Microgrids

An electron-based lithography technique for manufacturing microgrids, based on the procedure developed by Pinna et al. [15], has been used to generate microgrids on the microstructure of interest. Small rectangular volumes with dimensions $4 \times 10 \times 20$ mm were machined from the heat treated material. The specimens will be later inserted into a rectangular hole at the middle of a plane strain compression (PSC) sample (see section 2.3 describing the plane strain compression test). The microgrid process is adapted from the procedure described in [25] by replacing the metal sputtering and evaporation step by an appropriate etching of the sample. It is schematically summarized on Fig. 2. First, one of the two larger surfaces of each sample was prepared by grinding, polishing down to 1 μm and electro-etching with a 20 %-NaOH solution in order to reveal the two-phase microstructure. This step is needed in order to allow linking the strain to the underlying microstructure when analyzing the results. Second, an electro-sensitive PMMA-based resin was deposited on the prepared sample surface. The coated sample was annealed at 140°C to promote resin polymerization, adhesion and to improve the mechanical

Table 1 Chemical composition in %wt of the investigated duplex grade

Cr	Ni	Mo	Mn	Si	Cu	C	N
21.96	2.99	0.91	2.88	0.39	0.67	0.03	0.18

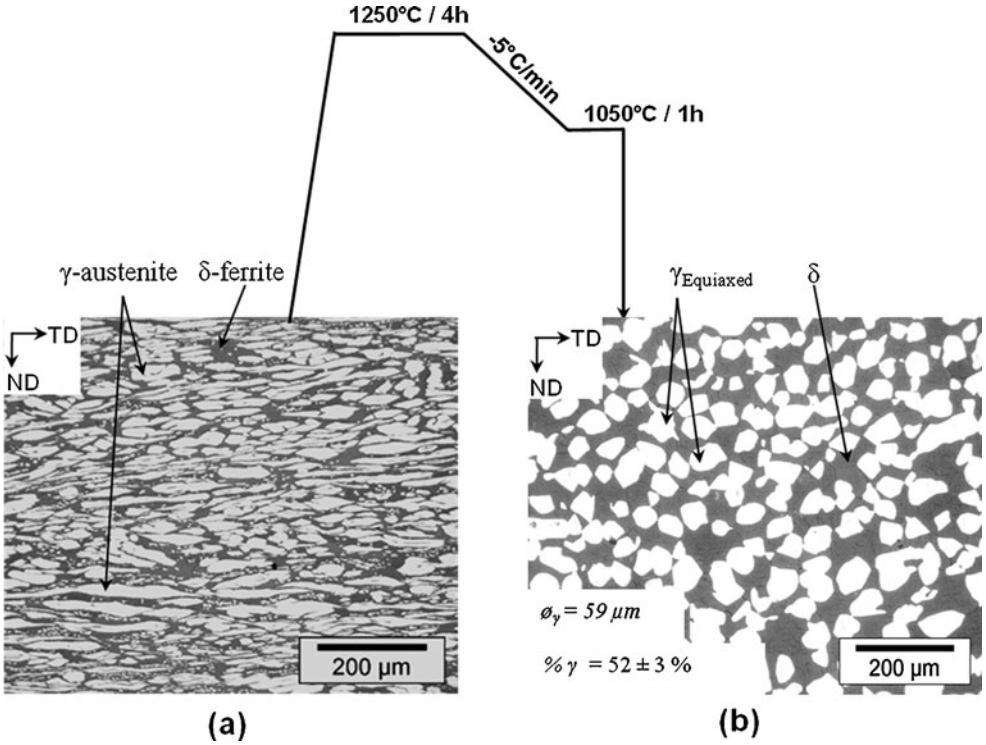

Fig. 1 Heat treatment used to generate an equiaxed austenite; (**a**) material in the as-received conditions; (**b**) microstructure resulting from the heat treatment

resistance of the film. The coated samples were then irradiated with the electron beam of a SEM, following the pattern of a square grid. After exposure, the channels of irradiated resin were removed using a solvent made of 75 %-propanol and 25 %-butanone (or Methy Ethyl Ketone). Third, the sample was electro-etched with a 40 %-HNO_3 solution, removing material only within the small areas without resin (the microgrid pattern). This step was undoubtedly the most critical because it required so much time to find the best etching conditions: solution, voltage and time. Finally, the remaining resin was dissolved in ethyl acetate, by means of ultrasonic cleaning, resulting in engraved microgrids with a step of about 5 µm.

After the fabrication of the microgrid, a low magnification-high definition image shown in Fig. 3(a) was obtained by SEM, covering the entire undeformed microgrid. Note that secondary electron mode was used because of its sensitivity to surface topography. High definition imaging (up to 4096× 3773 pixels) on a FEI Quanta 600 SEM was selected in order

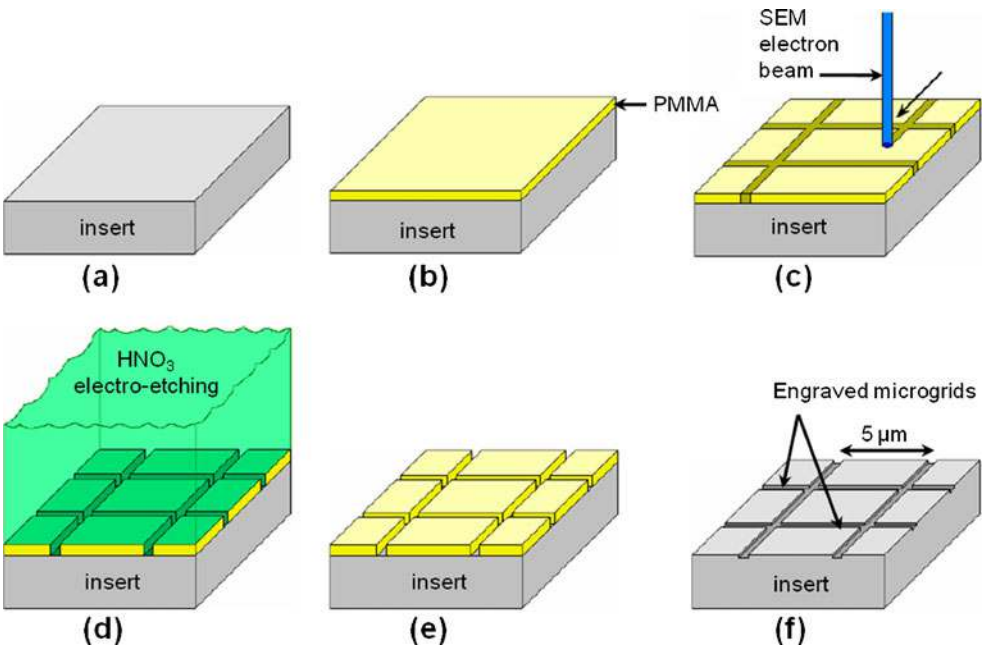

Fig. 2 Fabrication of the microgrids; (**a**) polishing and electro-etching; (**b**) coating with an electro-sensitive polymer; (**c**) irradiation of the resin with the electron beam; (**d**) dissolution of the irradiated polymer; (**e**) engraving by electro-etching; (**f**) dissolution of the remaining polymer [13]

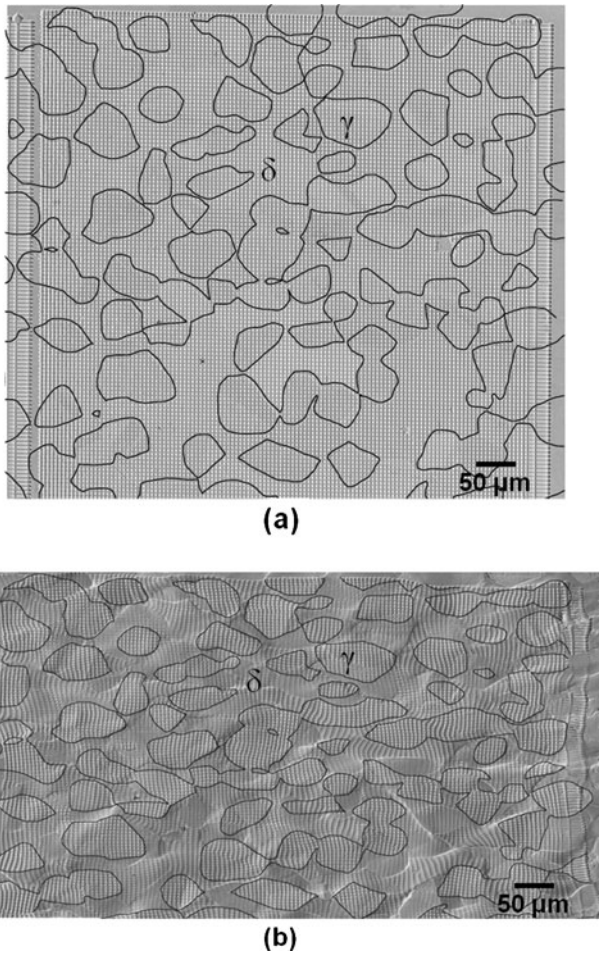

Fig. 3 SEM low magnification-high definition images; (**a**) before hot deformation; (**b**) after hot deformation; the contour of the δ/γ interfaces are highlighted with a *black line*

to combine a good description of the individual grids and a large field of view to improve statistical representativity of the local strain mapping. Pixel size was close to 150 nm. If the interphase boundaries can be extracted from such image, revealing also the grain boundaries turned out to be too difficult owing to experimental issues.

Plane Strain Compression Test

The microgrids engraved on the samples were deformed by high temperature plane strain compression (PSC), following the procedure developed by Pinna et al. [15]. The geometry of the PSC specimens is modified by machining a rectangular hole in the centre in order to protect the microgrids from oxidation and to locate them in the area where plane strain conditions are expected, as investigated in [35]. The procedure to assemble the modified PSC specimen and microgrid sample follows the different steps described in Fig. 4: (1) the microgrid specimen is welded to a polished plate made of the same material in order to protect the microgrid surface during the assembly within the PSC samples, the heat affected zone being controlled so that the microgrids and the microstructure are not modified; (2) the welded plates are inserted into the rectangular hole in the centre of the PSC specimen, with the microgrid surface parallel to the loading direction; (3) the inserts and the PSC samples are welded together on top and bottom to protect the microgrid from oxidation during the high temperature test.

The PSC specimen was quickly heated at 950°C (~20°C.s^{-1}), annealed for 30s at this temperature to ensure a homogeneous temperature field, and compressed with a thermo-mechanical compression machine (Servotest) to a reduction of 20 % ($\varepsilon_{eq}^{VonMises} = 0.24$, see equation (5)) at 1 s^{-1} nominal strain rate. The temperature and heating/cooling rate were controlled using a thermocouple located as close as possible to the microgrids in a small circular hole which was preliminary machined from the specimen side as indicated in Fig. 4(d). The specimen was immediately water-quenched after deformation in order to limit microstructural modifications such as phase transformation, recrystallization and grain growth.

Then, the microgrid sample was extracted from the PSC specimen, and the entire microgrid was analyzed in the SEM, in the same way as before deformation, see Fig. 3(b).

Strain Distribution Mapping

The comparison between the undeformed and the deformed state allows a quantitative characterization of the strain distribution. A fully automated digital image correlation analysis was not possible because of the presence of many small areas where the microgrids were damaged or exhibited too large variation of the local image contrast between the reference and the undeformed configuration. The local reliefs induced by the out-of-plane displacement as well as the slight oxidation which can occur during the thermo-mechanical process are responsible for the variations of the local image contrast. In these areas, the grey level conservation principle on which correlation technique relies is no longer valid. That is why the microgrid intersections were for the majority of them manually located using the software *CMV* developed at the laboratory LMS. This software combines DIC-based automatic pattern matching algorithms with a graphical user interface which allows a reasonably accurate and fast mouse-based manual positioning of point. Automatic procedures are used in areas where image characteristics are compatible with a direct application of these procedures; DIC principles can also be used to relocate more accurately points which have been approximately set manually. This software has originally been developed for the work described in [15] to process the strongly deformed

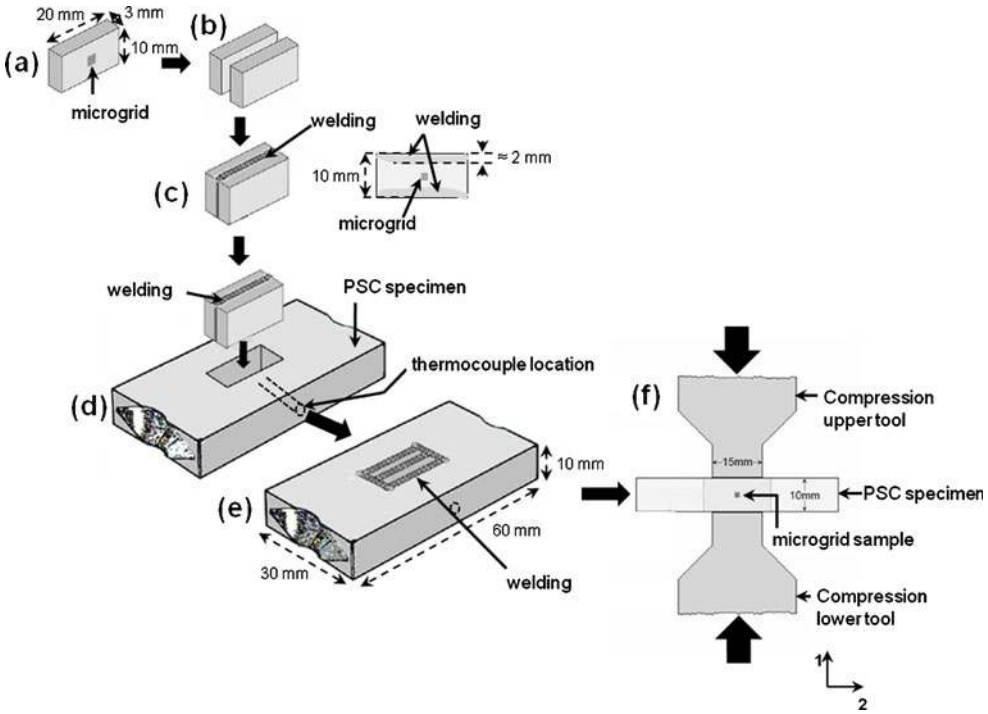

Fig. 4 Preparation of the plane strain compression specimen; (**a**) microgrid sample; (**b**) face to face with a similar polished sample and (**c**) welding; (**d**) assembly within a modified plane strain compression specimen; (**e**) welding at the top and bottom areas; and (**f**) schematic view of the microgrid sample inserted into the plane strain compression specimen and the compression tools during the tests

SEM images obtained in that context, which could not be fully processed with automatic DIC routines [31]. Various developments have been added since then various applications [17, 29, 30, 33].

This software provides the in-plane displacement components of each microgrid intersection, from which the in-plane components of the local, per-phase average or overall transformation gradient tensor $\overline{\overline{F}}$ can be calculated. The local transformation gradient at a given grid intersection p is computed as the average of the true local gradient over a small surface S^p around the grid intersection. The chosen surface is a polygonal surface where vertices are neighbours of the considered grid intersection. Let x be the position of a grid intersection in the deformed configuration, Σ^p the boundary of S^p and ν^p its normal. The local transformation gradient can then be computed using a contour integral:

$$F^p = \frac{1}{S^p} \int_{\Sigma^p} x \otimes \nu^p dl, \tag{1}$$

$\nu^p\ dl$ is constant on a segment of Σ^p and a local linear interpolation between intersections is assumed. Several choices are possible for the polygonal surface S^p, see [25]. In the present study, a four-neighbours scheme is used, resulting in a gage length for local strain evaluations of $\sqrt{2}$ grid intersections, i.e. 7 μm. The procedure to compute local gradients as averages over a small domain around the considered grid intersection can be used to compute per-phase average gradients using the polygonal lines defined in Fig. 5. The out-of-plane displacement cannot be measured directly. Its variations with the in-plane coordinates are assumed to be negligible for the computation of the in-plane components of the logarithmic strain tensor $\overline{\overline{\varepsilon^{\log}}}$. This assumption is equivalent to assume that the surface of observation is a principal plane of the strain tensor. It seems appropriate from a macroscopic point of view since plane strain conditions are globally enforced at the location of the plane of interest. As a first approximation, it is also reasonable for the per-phase average strain since, on average, the deformation state of a phase keeps the same symmetry as the macroscopic deformation. Indeed, the local phase distribution on a representative domain is statistically symmetric with respect to the plane of observation. This assumption is probably not justified locally at a particular point within each phase, since a three-dimensional state of deformation develops because of the heterogeneity of the microstructure and the anisotropy of the plastic deformation at the grain scale.

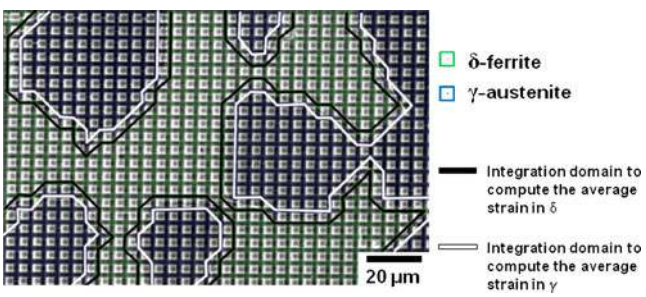

Fig. 5 Example of a correspondence between the microgrids and the underlying microstructure with phase boundaries

The in-plane components of the average or local logarithmic strain tensor, $\overline{\overline{\varepsilon^{\log}}}$ can be derived from the multiplicative decomposition of the average or local gradient tensor as

$$\overline{\overline{F}} = \overline{\overline{R}} \cdot \overline{\overline{U}}, \tag{2}$$

where $\overline{\overline{R}}$ is the rigid rotation tensor and $\overline{\overline{U}}$ is the distortion tensor. The distortion tensor $\overline{\overline{U}}$ can then be diagonalized in an orthogonal base as follows

$$\overline{\overline{U}} = \overline{\overline{Q^t}} \cdot \overline{\overline{D}} \cdot \overline{\overline{Q}}, \tag{3}$$

where $\overline{\overline{D}}$ is the diagonal tensor, $\overline{\overline{Q}}$ is a tensor giving the orientation of the principal directions of the distortion and $\overline{\overline{Q^t}}$ is the transpose tensor of $\overline{\overline{Q}}$. The logarithmic strain tensor is finally computed as

$$\overline{\overline{\varepsilon^{\log}}} = \overline{\overline{Q^t}} \cdot \ln \overline{\overline{D}} \cdot \overline{\overline{Q}}. \tag{4}$$

The Von Mises equivalent strain was determined using the following relationship

$$\varepsilon_{eq}^{VonMises} = \sqrt{\frac{2}{3}\left(\varepsilon_{11}^2 + \varepsilon_{22}^2 + \varepsilon_{33}^2 + 2\varepsilon_{12}^2\right)}, \tag{5}$$

where ε_{11}, ε_{22}, ε_{33} and ε_{12} are the local strain in the direction 1 (normal direction), the local strain in the direction 2 (rolling direction), the local strain in the direction 3 (out-of-plane or transverse direction) and the shear component, respectively. The ε_{33} component is deduced from the assumption that the transformation is isochoric: *det F=1*.

In order to estimate the per-phase behaviour, the strain maps must be linked to the underlying microstructure. In Fig. 5, two different polygonal lines joining microgrids intersections are drawn representing the boundaries used to locate each phase and to relate each intersection to one of the phase. The black line corresponds to the limits of the integration field to determine the average deformation in the ferrite, and the white line defines the boundaries that permit to estimate the average strain in the austenite. In order to evaluate the error related to the manual location of the microgrid intersections, the micro-scale strain distribution of the same region has been determined several times. The per-phase average strains were not significantly affected since after each analysis the values did not differ from more than ±0.002. The local strains can be more significantly affected but the error was still acceptable equal to ±0.010. More details about the calculations of the strains and about error estimations with the microgrid technique can be found in [25].

Results and Discussions

Macroscopic Stress–Strain Curve

Figure 6 shows the macroscopic equivalent stress–strain curve obtained from the plane strain compression test after post-processing the raw data as described in [36]. This response is representative of the true material since the plane strain compression specimen and the inserts were machined from the same material. The stress–strain curve exhibits a classical shape with an elastic stage, a yield stress equal to about 110 MPa, followed by strain hardening until the flow stress reaches a steady state value equal to about 170 MPa.

Micro-scale Strain Analysis

A representative area was selected from the large SEM picture of the deformed microgrids, and the displacements of the grid intersections with respect to the undeformed configuration were used to calculate the distribution of the local strain components and of the Von Mises equivalent strain. The calculated data were represented as color maps corresponding to different levels of strain. The corresponding microstructure, in the undeformed configuration, was edited to extract the interphase boundaries. The boundaries were then superimposed to the color maps in order to reveal clearly the link with the background microstructure. The strain maps are shown in Fig. 7 based on 10464 microgrid intersections.

In previous studies [11, 15, 16], the technique was applied to laboratory-made Fe-Cr-Ni alloys without any significant amount of other alloying elements such as N or Mo. The strain distributions were determined only over small areas (~100×100 μm^2), including no more than 4–5 grains of ferrite and austenite. In addition, as the average grain size was about 20 μm with a 5 μm grid-step, the resolution

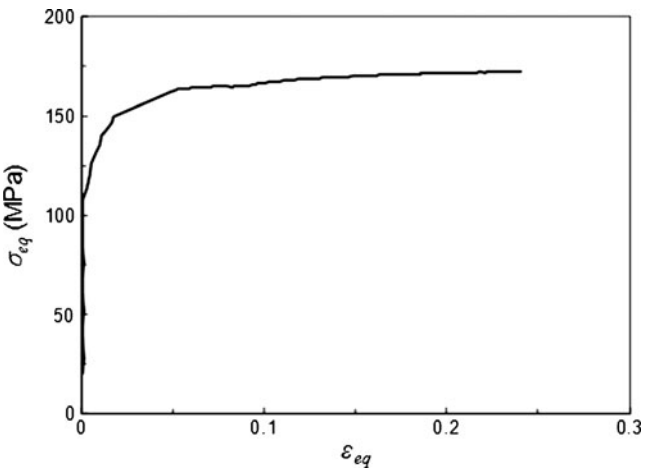

Fig. 6 Macroscopic equivalent stress strain curve corresponding to plane strain compression performed at 950°C with a strain rate equal to 1 s^{-1} up to a reduction of 20 %

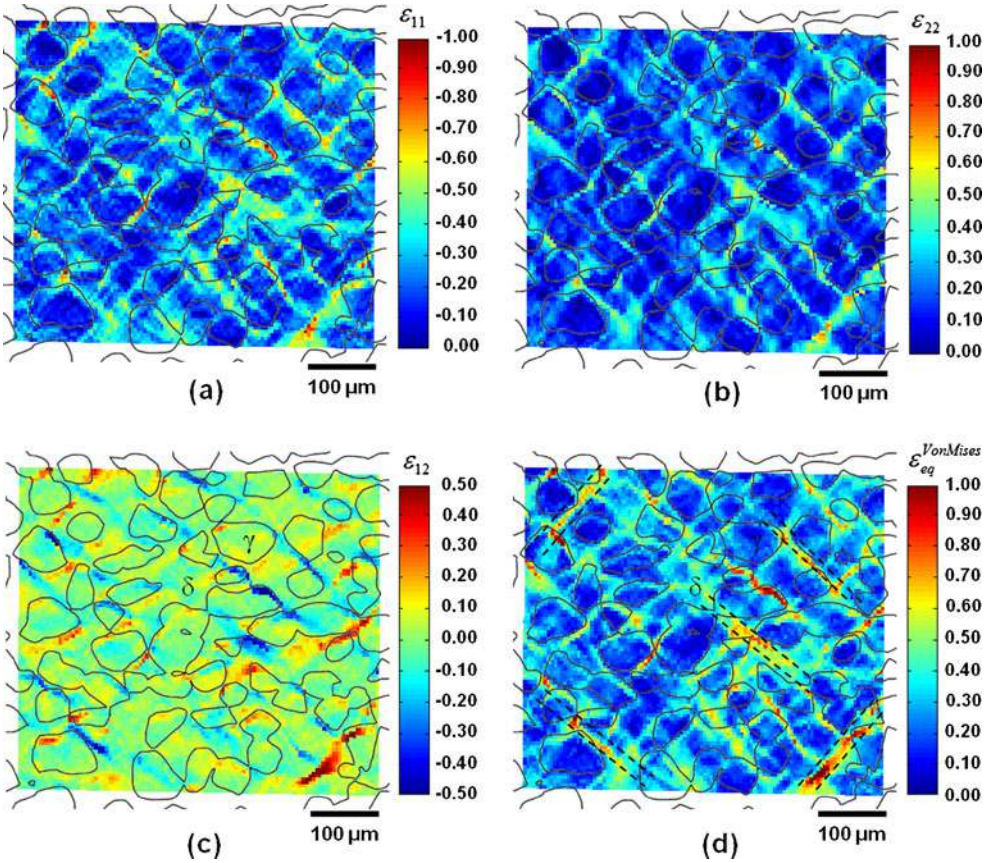

Fig. 7 Logarithmic strain distribution maps after plane strain compression; (**a**) ε_{11}; (**b**) ε_{22}; (**c**) ε_{12}; (**d**) ε_{eq}; the strain maps are superimposed with the undeformed microstructure; the compression axis corresponds to the vertical axis

obtained on the strain maps was limited. In other words, it means that the number of grid intersections per grain (points where the strains are estimated) was limited. In the present investigation, some significant improvements have been carried out, the most important are listed below.

- A more realistic material is used: an industrial DSS containing a large number of alloying elements which a few of them such as Mo and N are known to significantly affect the mechanical properties of the different phases due to the partition of alloying elements. For instance, N is a strong austenite stabilizer and tends to strengthen the austenitic phase.
- The strain distribution are determined over larger areas (500×500 µm^2) in a such manner as to include a representative volume of the entire microstructure and also to permit a more statistically analysis.
- Note that the grid-step (5 µm) used in this present investigation is relatively small compared to the microstructure characteristic lengths: the average austenite grain size is equal to 60 µm. This last comment suggests that strain maps with a good resolution can be determined, particularly in the vicinity of the δ/γ interphase boundaries.
- Finally, the innovative aspect of the present investigation lies on the different methods suggested to quantitatively characterize the strain partitioning. For instance, the quantitative analysis of the strain distribution is not limited to the computations of the average strain per phase, see section 3.2.2 dealing with the quantitative analysis.

Qualitative analysis

Some general qualitative considerations concerning the deformation patterns can be made by observing the strain maps and the micrograph with the deformed microgrids.

First of all, the strain maps show that the deformation is heterogeneous with some areas only slightly deformed and others strongly deformed, see Fig. 7. SEM micrographs of the deformed microgrids confirm these considerations. Furthermore, the most deformed regions in the microstructures are almost always situated in the vicinity of the δ/γ interphase boundaries or in the ferrite. The most deformed regions (red color in the strain maps) correspond to ferrite. The deformation is thus accommodated more by the ferrite than by the austenite. Locally, the ratio $\varepsilon_{eq}^{\delta} \Big/ \varepsilon_{eq}^{\gamma}$ of the deformation in both phases at the neighborhood of the interphase boundary fluctuates between 2 and 3, and in a few areas the ratio can get up to 5.

The observation of the deformed microgrids reveals the occurrence of a sliding mechanism at some δ/γ interphase

boundaries, see Fig. 8(a). This result confirms the characterizations carried out by Pinol-Juez et al. [10] and Pinna et al. [15]. Since the local strains forming the strain distributions are computed from the displacement of the microgrid intersections, when a δ/γ interphase boundary crosses a grid square, it opens the possibility of inaccurate estimations of the strains in the vicinity of the boundary. In some locations, the shear deformation around a δ/γ interphase boundary can be relaxed if sliding takes place at such interfaces, as shown in Fig. 8(a). However, if we look only at the positions of the microgrid intersections after deformation (see black dots in Fig. 8(a)), it will be interpreted by the calculations as a shear strain higher than the actual one (see white lines in Fig. 8 (a)). The extent of the sliding varied from one boundary to another, and did not seem to have a direct relation with geometrical factors such as the length and shape of the boundaries. It could change from one place to another along the same boundary, probably due to the interactions between grains/phases which varies the constraint at different positions along the boundary. It is considered that high strains values located in the vicinity of the δ/γ interphase boundaries must be carefully analyzed. One solution consists in comparing the strain maps with the deformed microstructure in order to find out if sliding has not occurred at the interphase boundaries, and confirm that they are genuine heavily deformed locations.

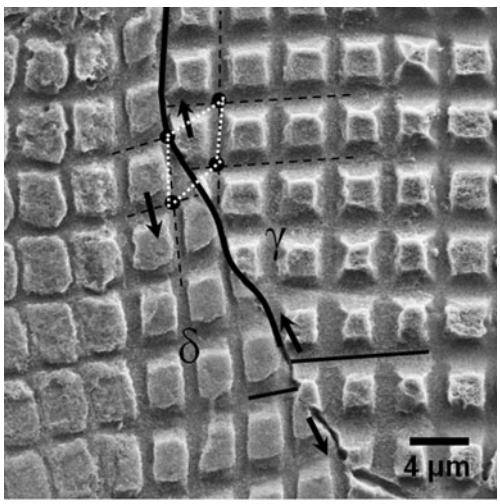

(a)

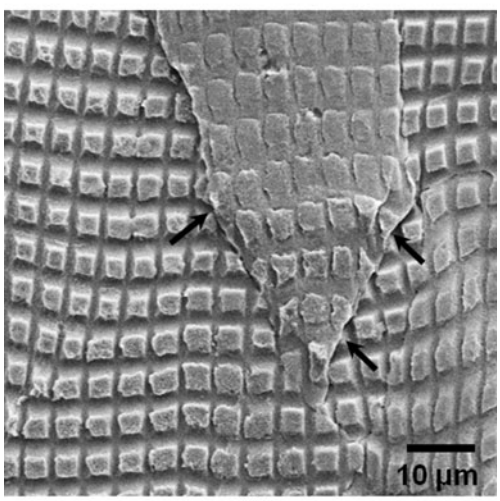

(b)

Fig. 8 SEM micrographs illustrating two important features of the deformation pattern; (**a**) sliding at the interphase boundary; (**b**) out-of-plane displacement, the arrows emphasize the step at the interphase boundary

Table 2 Average logarithmic deformation per phase in the microstructure of interest; the brackets mean "on average"

	$<\varepsilon_{11}>$	$<\varepsilon_{22}>$	$<\varepsilon_{12}>$	$<\varepsilon_{33}>$	$\varepsilon_{eq}^{VonMises}$
Overall	−0.266	0.218	0.003	0.048	0.284
Austenite γ	−0.185	0.149	0.002	0.036	0.196
Ferrite δ	−0.310	0.260	0.007	0.050	0.333

Another deformation feature observed in Fig. 8(b) is the presence of steps at some deformed grain or interphase boundaries. This feature was presumably caused by the out of-plane displacement of the microgrid surface during deformation.

The strain maps, especially the shear strain map (Fig. 7(c)) highlight also the development of shear bands, see the dotted lines in Fig. 7(d). The development of these shear bands seems to depend on the distribution of the austenite grains.

All these deformation features allow a better qualitative understanding of the mechanisms involved in the high temperature deformation of duplex stainless steels. Additional analysis is needed to generate a more quantitative treatment of the strain partitioning in both microstructures.

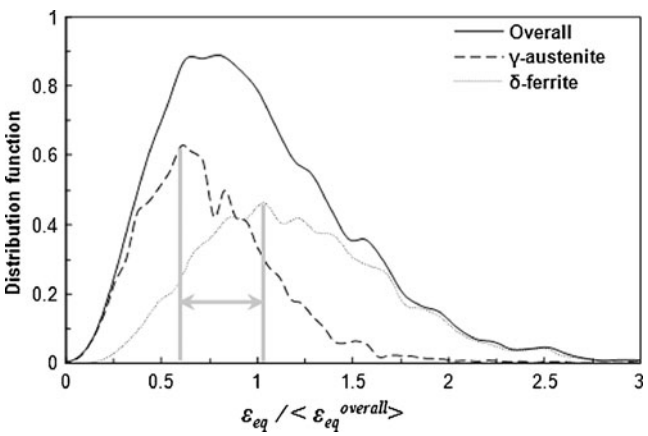

Fig. 9 Strain distribution functions relative to the volume fraction of phase

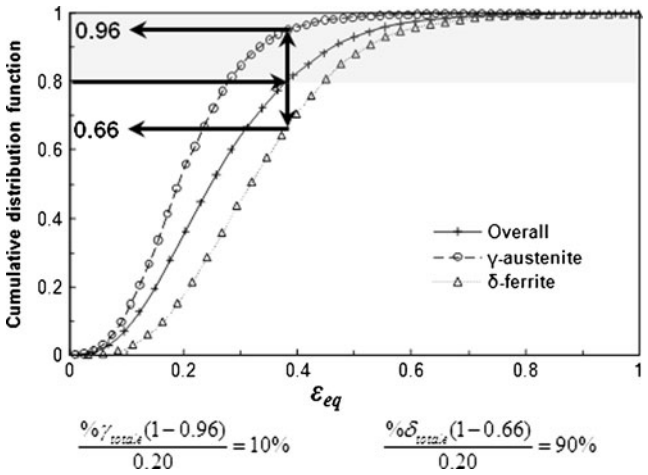

Fig. 10 Strain cumulative distribution functions normalized by the volume fraction of phase

Quantitative analysis

Several options are available to provide quantitative results about the strain partitioning. An overview of these options is given in this section.

First of all, the average deformation per phase for both microstructures can be computed as summarized in Table 2. A relevant parameter which allows quantifying the strain partitioning is the ratio between the average deformation in the ferrite divided by the average deformation in the austenite. The results show that the ferrite accommodates more deformation compared to the austenite: on average, the ferrite is deformed ~70 % more than the austenite. These results can be discussed and compared with literature data. The study of the strain partitioning in DSS at room temperature has been attempted by several researchers, see examples in [12, 14]. However, data about the high temperature strain heterogeneities in DSS are limited, probably because it is much more challenging. Indeed, at high temperature, additionally to the difficulties related to the high-temperature microstructure control for materials affected by phase transformations, the speckle or grid material must exhibit an excellent resistance to thermal and environmental damage. In addition, solutions to avoid the excessive oxidation of the markers have to be found. And finally, the markers should exhibit a good high temperature deformability to reveal the material deformation without undesirable cracking or detachment of the markers. Kempf et al. [12] have investigated the microscale strain distribution at room temperature in a 2205-DSS deformed plastically under tension using a grid technique. They pointed out significant differences in the mechanical behaviour of both phases. For instance, considering the strain in the loading direction, the austenite was found to deform more than the ferritic phase. In addition, significant strain gradients were detected close to the δ/γ interphase boundaries confirming the observations of the present study. Evrard et al. [14] have studied the intraphase and intergranular strain heterogeneities in a 2507-DSS using digital image correlation (DIC). The authors reported that the average strain in the tension direction was about 20 % larger in the austenitic phase in comparison with the ferritic phase. These results show that at room temperature the austenite seems to accommodate more deformation compared to the ferrite.

On the contrary, at high temperature, Duprez et al. [3] showed that the strain seems to be preferentially localized in the ferritic phase. Based on the dimensional evolutions of the grains during hot rolling, they have estimated that the strain ratio between the constituent phases ($\varepsilon^{\delta}/\varepsilon^{\gamma}$) was about 3 after 30 %-thickness reduction in a 2205-DSS. Although this method provides quantitative information on the high temperature strain partitioning between ferrite and austenite in a DSS, this method turns out to be rather inaccurate as it neglects shear strains. In addition, the results give only an average strain value per phase and do not permit to see how the strains are distributed in the microstructure. The results of the present investigation as well as the results previously published in [11] confirm a larger accommodation of the strain by the ferritic phase. However, there are some quantitative differences in terms of strain partitioning considering these different investigations. A strain ratio of 3 is reported by Duprez et al. [3], such value can be only locally reached (see for example on Fig. 7(d) the areas where blue regions are close to red regions), but on average this strain ratio is much lower. Indeed, Hernandez-Castillo et al. [11] indicated larger deformation, about 30–40 % in the soft ferritic matrix compared to that in the austenitic phase ($\varepsilon^{\delta}/\varepsilon^{\gamma}$=1.3–1.4) whereas in the present study the ferrite is deformed ~70 % more than the austenite ($\varepsilon^{\delta}/\varepsilon^{\gamma}$.=1.7). These differences in terms of strain partitioning could be attributed to a difference of chemical composition between the investigated materials. For instance, the DSS investigated in this work exhibits a significantly higher amount of nitrogen compared to that studied in [11], and N distributes preferentially into the austenite leading to a significant strengthening of the austenitic phase.

The overall equivalent strain calculated from the deformation strain maps (0.284) differs from the applied macroscopic equivalent strain (0.240) because of a moderate strain gradient in the deformation of the overall plane strain compression specimen with slightly larger values in the centre

Table 3 Ferrite content (*%δ*) in the areas the most deformed

X% the most strained	1 %	5 %	10 %	15 %	20 %	25 %	30 %
%δ	92±1	92±1	90±1	93±1	90±1	87±1	84±1

[35, 37, 38]. The assumption of a constant out-of-plane displacement seems to be justified for the overall and the per-phase average logarithmic strain. Indeed, the values found for ε_{33} can be neglected compared to the other deformation components.

Another way to characterize the strain heterogeneity is to plot the strain distribution functions as shown in Fig. 9. These distribution functions give the probability that the local equivalent strain is equal to a given value of the deformation. The strain distribution functions of the ferrite and the overall strain distribution functions are superimposed for the large strain values. It means that the most deformed regions are always located in the ferrite. Focusing on low strain values, the strain distribution functions of the austenite and the overall strain distribution function are superimposed confirming that the less distorted regions are located in the austenite.

The cumulative deformation distribution functions normalized by the volume fraction given in Fig. 10 are deduced from the strain distribution functions by integration. These curves allow estimating the ferrite and austenite contents involved in the X% of most deformed regions of the microstructure, see Table 3. In Fig. 10, an example is given to illustrate the method used to estimate graphically the ferrite and austenite contents in the 20 % most deformed regions. The results summarized in Table 3 confirm that the regions the most deformed regions essentially consist of ferrite. For instance, the 10 % of the material the most deformed consist of 90 % of ferrite and only 10 % of austenite, see Table 3.

Conclusions

A micro-extensometry technique using square grids engraved on flat specimens has been successfully applied for the measurement of the local deformation field in a duplex stainless steels deformed at 950°C under plane strain conditions. The resulting deformation patterns and strain maps provide the quantitative distribution of the in-plane strain components at the scale of the microstructure. The results revealed that the strain is heterogeneously distributed with a strong localization of the deformation into shear bands within the ferrite. Microstructural observations of the deformed microgrids showed that part of the deformation can be accommodated by the sliding of some δ/γ interphase boundaries. At the vicinity of the δ/γ interphase boundaries, the ratio between the local strain in the ferrite over the local strain in the austenite can reach a value of 5. This observation probably explains why voids always nucleate by decohesion of the δ/γ interphase boundaries, as observed in many earlier studies on duplex [5, 10, 39] or ferritic stainless steels [40, 41].

The application of the micro grids technique opens new avenues for the investigation of multiphase microstructures deformed at high temperature, such as duplex stainless steels (austenite-ferrite microstructure) during hot rolling. The application of this technique to estimate accurately the strain partitioning in hot rolled duplex stainless steels will permit experimental validation of models dedicated to the prediction of the deformation of austenite-ferrite microstructures.

Acknowledgements The authors thank APERAM and the Centre National de la Recherche Scientifique (CNRS) for supporting this work. The authors are respectively grateful to Alain Lemoulec from SIMaP (Laboratoire de Science et Ingénierie des Matériaux et Procédés) and John Hinton from IMMPETUS (Institute for Microstructural and Mechanical Process Engineering: The University of Sheffield) for their help for the processing of the welding and the hot mechanical tests. The Quanta 600 SEM of the Laboratoire de Mécanique des Solides used for imaging and microgrid generation has been acquired with the help of the SESAME funding (Soutien aux Equipes Scientifiques pour l'Acquisition de Moyens Expérimentaux) program of the "Région Ile-de-France".

References

1. Charles J (2008) A review after DSS'07 held in Grado. Steel Res Int 79:455–465
2. Liou HY, Pan YT, Hsieh RL, Tsai WT (2001) Effect of the alloying elements on the mechanical properties and corrosion behaviors of 2205 duplex stailess steels. J Mater Eng Perform 10:231–241
3. Duprez L, De Cooman BC, Akdut N (2002) High-temperature stress and strain partitioning in duplex stainless steel. Z Metallkde 93:236–243
4. Iza-Mendia A, Gutierrez I (2007) Factors affecting the hot workability of duplex stainless steels. Proceedings of the Duplex 2007 International Conference and Expo, Grado, Italy, CD only
5. Iza-Mendia A, Pinol-Juez A, Urcola JJ, Gutierrez I (1998) Microstructural and mechanical behavior of a duplex stainless steel under hot working conditions. Metall Mater Trans A 29:2975–2986
6. Dehghan-Manshadi A, Hodgson PD (2008) Effect of delta-ferrite co-existence on hot deformation and recrystallization of austenite. J Mater Sci 43:6272–6277
7. Cizek P, Wynne BP (1997) A mechanism of ferrite softening ina duplex stainless steel deformed in hot torsion. Mater Sci Eng A 230:88–94
8. Evangelista E, McQueen HJ, Niewczas M, Cabibbo M (2004) Hot workability of 2304 and 2205 duplex stainless steels. Can Metall Q 43:339–354
9. Liu J, Fan GW, Han PD, Liu JS, Gao JQ, Yang JF (2009) Effect of the nitrogen content on the hot dutility during hot deformation of stainless steels. Eco-Materials Processing and Design X 620–622:161–164
10. Pinol-Juez A, Iza-Mendia A, Gutierrez I (2000) Delta/gamma interface boundary sliding as a mechanism for strain accomodation during hot deformation in a duplex stainless steel. Metall Mater Trans A 31:1671–1677
11. Hernandez-Castillo LE, Beynon JH, Pinna C, Van der Zwaag S (2005) Micro-scale strain distribution in hot-worked duplex stainless steel. Steel Res Int 76:137–141
12. Kempf D, Vignal V, Cailletaud G, Oltra R, Weeber JC, Finot E (2007) High spatial resolution strain measurements at the surface of duplex stainless steels. Phil Mag 87:1379–1399

13. Pin Peng R, Chai G, Jia N, Wang YD, Johansson S (2008) Micromechanical interactions in a super duplex stainless steel subjected to low cycle fatigue loading. Fat Fract Eng Mater Struct 31:892–901
14. Evrard P, El Bartali A, Aubin V, Rey C, Degallaix S, Kondo D (2010) Influence of boundary conditions on bi-phased polycrystal microstructure calculation. Int J Sol Struct 47:1979–1986
15. Pinna C, Beynon JH, Sellars CM, Bornert M (2000) Experimental investigation and micromechanical modeling of the hot deformation of duplex stainless steels. Proceedings of the Int. Conf. on Mathematical Modelling in Metal Processing and Manufacturing-COM 2000, Ottawa, Ontario, CD only
16. Hernandez-Castillo LE (2005) Determination of micro-scale strain distribution in hot-worked steel microstructures. Thesis, Department of Engineering Materials, University of Sheffield, United-Kingdom
17. Rupin N (2007) Déformation à chaud de métaux biphasés : modélisations théoriques et confrontations expérimentales. Thesis, Laboratoire de Mécanique des Solides, Ecole Polytechnique, France
18. Unckel H (1937) J Inst Met 61:171
19. Al Jouni FE (1983) Hot deformation of two phase stainless steels. Thesis, Department of Engineering Materials, University of Sheffield, United-Kingdom
20. Petrovic JJ, Vasudevan AK (1978) Rolling deformation of 2-ductile-phase Ag-Ni alloys. Mater Sci Eng A 34:53–59
21. Cai XL, Feng J, Owen WS (1985) The dependence of some tensile and fatigue properties of a dual-phase steel on its microstructure. Metall Mater Trans A 16:1405–1415
22. Raabe GI (2005) Plastic flow at equal channel angular processing in parallel channels. Mater Sci Eng A 410–411:230–233
23. Wang ZJ, Liu Y (2010) Investigation on deformationbeahvior of sheet metals in viscous pressure bulging based on EPSI. J Mater Process Technol 210:1536–1544
24. Baudulescu C, Grediac M, Mathias JD (2009) Investigation of the grid method for accuratein-plane strain measurement. Meas Sci Technol 20:095102
25. Allais L, Bornert M, Bretheau T, Caldemaison D (1994) Experimental characterization of the local strain field in a heterogeneous elastoplastic material. Acta Metall Mater 42:3865–3880
26. Soula A, Locq D, Boivin D, Renollet Y, Caron P, Brechet Y (2010) Quantitative evaluation of high temperature deformation mechanisms: a specific microgrid extensometry technique coupled with EBSD analysis. J Mater Sci 45:5649–5659
27. Ghadbeigi H, Pinna C, Celotto S, Yates JR (2010) Local plastic strain evolution in a high strength dual-phase steel. Mater Sci Eng A 527:5026–5032
28. Kang JD, Ososkov Y, Embury JD, Wilkinson DS (2007) Digital image correlation studies for microscopic strain distribution and damage in dual-phase steels. Scr Mater 56:999–1002
29. Heripre E, Dexet M, Crepin J, Gelebart L, Roos A, Bornert M, Caldemaison D (2007) Coupling between experimental measurements and polycrystal finite element calculations for micromechanical study of metallic materials. Int J Plasticity 23:1512–1539
30. Soppa E, Doumalin P, Binkele P, Wiesendanger T, Bornert M, Schmauder S (2001) Experimental and numerical characterisation of in-plane deformation in two-phase materials. Comput Mater Sci 21:261–275
31. Doumalin P, Bornert M (2000) Micromechanical applications of digital image correlation techniques. Proceedings Interferometry in Speckle Light, Theory and Applications, EPFL, Lausanne, Springer-Verlag, Berlin, Germany, pp. 67–74
32. Jacques PJ, Furnemont Q, Lani F, Pardoen T, Delannay F (2007) Multiscale mechanics of TRIP-assisted multiphase steels: I. Characterization and mechanical testing. Acta Mater 55:3681–3693
33. Bornert M, Vales F, Gharbi H, Minh DN (2010) Multiscale full field strain measurements for micromechanical investigations in the hydromechanical behaviour of clayey rocks. Strain 46:33–46
34. Martin G, Veron M, Chehab B, Fourmentin R, Mithieux JD, Yerra SK, Delannay L, Pardoen T, Brechet Y (2011) Duplex stainless steels microstructural developments as model microstructures for hot ductility investigations. Solid State Phenom 172–174:350–356
35. Boldetti C (2006) Multi-scale measurement and modelling of large deformation of structural metals during thermomechanical processing. Thesis, Department of Mechanical Engineering, University of Sheffield, United-Kingdom
36. Loveday MS, Mahon GJ, Roebuck B, Lacey AJ, Palmiere EJ, Sellars CM, Van der Winden MR (2006) Measurement of flow stress in hot plane strain compression tests. Mater High Temp 23:85–118
37. Beynon JH, Sellars CM (1985) Strain distribution patterns during plane strain compression. J Test Eval 13:28–38
38. Mirza MS, Sellars CM (2001) Modelling the hot plane strain compression test Part I—Effect of specimen geometry, strain rate, and friction on deformation. Mater Sci Technol 17:1133–1141
39. Martin G, Yerra SK, Bréchet Y, Véron M, Mithieux JD, Delannay L, Chéhab B, Pardoen T (2012) A macro and micromechanics investigation of hot cracking in duplex steels. Acta Mater. doi:10.1016/j.actamat.2012.03.040
40. Chehab B, Brechet Y, Glez JC, Jacques PJ, Mithieux JD, Veron M, Pardoen T (2006) Characterization of the high temperature tearing resistance using the essential work of fracture-Application to dual phase ferritic stainless steels. Scr Mater 55:999–1002
41. Chehab B, Brechet Y, Veron M, Jacques PJ, Parry G, Mithieux JD, Glez JC, Pardoen T (2010) Micromechanics of high temperature damage in dual-phase stainless steel. Acta Mater 58:626–637